ELSEVIER

Contents lists available at ScienceDirect

Soil Dynamics and Earthquake Engineering

journal homepage: www.elsevier.com/locate/soildyn





Assessment of fabric characteristics with the development of sand liquefaction in cyclic triaxial tests: A DEM study

Jiajin Zhao ^a, Zhehao Zhu ^{a,*}, Dexuan Zhang ^a, Hao Wang ^b, Xi Li ^c

- ^a School of Civil Engineering, Shanghai Normal University, Shanghai, 201418, China
- ^b Laboratoire Navier/CERMES, École des Ponts ParisTech, Cité Descartes, Champs-sur-Marne, 77420, France
- ^c School of Traffic and Transportation Engineering, Changsha University of Science and Technology, Changsha, Hunan, 410114, China

ARTICLE INFO

Keywords: Sand liquefaction DEM Cyclic triaxial test Fabric characteristics Anisotropy degree

ABSTRACT

This paper studies fabric properties with the evolution of sand liquefaction by performing a series of 3D constant-volume cyclic triaxial DEM tests. With calibrated parameters for HN31 sand, the consistency between the obtained DEM results and the counterpart experiments is presented. The evolution of fabric characteristics is then assessed with the coordination number and mechanical coordination number, respectively. For liquefaction issues, the conventional coordination number outperforms the mechanical one since the floating particles with the number of contacts less than or equal to 1 can be fully considered. To analyse the complex inter-particle contacts in a granular assembly, the second-order contact normal fabric tensor is briefly introduced with its important mathematical properties. The second invariant of its deviatoric part can prove to be a proper index describing the degree of anisotropy in the principal fabric space spanned by the three eigenvectors belonging to this tensor. Following the direction of the applied loading, the fabric anisotropy accumulates in a gradual manner and finally reaches a threshold value corresponding to liquefaction triggering on the macro scale. This value is fabric-dependent and thus independent of loading intensity. For gaining a complete insight of sand liquefaction on both the micro and macro scales, the shear strain can act as a bridge to describe the evolution of coordination number and the anisotropy degree, respectively.

1. Introduction

Under seismic loading, saturated sand deposits are highly sensitive to liquefaction at locations where the ground water level is shallow. In such a case, soil elements experience a transient loss of shear strength and even exhibit a liquid-like behaviour. A large and growing body of field evidence [1–4] has revealed that spectacular examples of engineering failures can be ascribed to this natural phenomenon.

Since the 1964 Niigata earthquake in Japan, research activities based on triaxial tests for sand liquefaction have been initiated and fruitful experimental results have been reported in the literature. As far as granular material is concerned, the change of fabric characteristics within a sand element is a crucial factor in comprehending the evolution of sand liquefaction. For instance, the experimental evidence provided by Ye [5] suggested that even a small pre-shear strain within the range of 0.1%–5% is capable of greatly disturbing the initial soil fabric, thereby altering the liquefaction brittleness. In shaking table tests involving sand liquefaction, the particle long-axis orientation has been the subject of

much systematic investigation. The mesoscopic structures identified by the digital image processing technique [6] have conclusively shown that a granular structure becomes much more prone to liquefaction collapse as the long-axis of sand particles tend to be more vertical. More recently, stress-induced anisotropy has been proven to be a prominent factor affecting reliquefaction resistance [7]. Yet, the concept of a triaxial specimen over a representative elementary volume (REV) only provides a means of performing macroscopic measures in the description of sand liquefaction. For a granular assembly containing uncountable particles and contacts, the state-of-the-art measurement technology used in the laboratory still falls short of achieving an intact and exact measurement of fabric properties directly with the progression of shearing. As an alternative, the DEM (discrete element method [8]) has been extensively applied in the study of liquefaction. Such a method offers another perspective on this topic by simulating granular materials with its discrete nature. It has evolved into a powerful tool for capturing both the monotonic and cyclic behaviours of sand with the consideration of critical state soil mechanics [9–16]. Meanwhile, investigating soil fabric

^{*} Corresponding author. School of Civil Engineering Shanghai Normal University, China. *E-mail addresses*: zhuzhehao@shnu.edu.cn, zhehao.zhu@enpc.fr (Z. Zhu).

through DEM simulations has become a primary objective of much research. In a DEM study examining the impact of initial soil fabric [17], sand specimens were fabricated with the identical initial void ratio but subjected to different pre-shearing processes. Compared with the isotropic specimen without undergoing pre-shearing process, those owing a higher initial anisotropic degree become much more prone to liquefaction initiation. This can be explained by the fact that an anisotropic specimen usually tends to deform along its weaker direction, resulting in a decreased resistance to liquefaction. In contrast, an isotropic specimen potentially exhibits the same strength in all directions, thereby displaying the greatest liquefaction resistance [18]. Yimsiri [19] has furnished a comprehensive summary of fabric evolution during undrained shearing, emphasizing a pronounced change in fabric anisotropy upon reaching the maximum excess pore water pressure (namely, the transition from contractiveness to dilatancy). Once dilatancy occurs, the remnants of initial fabric structure become more or less erased. This is the reason for the diminished influence of the initial fabric on subsequent shearing.

In soil mechanics, the void ratio e, defined as the volume of voids divided by the volume of solids, is the most straightforward variable to characterize a given soil fabric and describes how dense the particle packing is. However, two granular systems with the same e can possibly have two different spatial distribution features. The void ratio is usually unable to express any fabric anisotropy and other intrinsic variables should be sought. For instance, the regular void ratio e cannot specify the mechanical contribution of fine particles in binary sand-fines mixtures [20,21]. This is because it solely accounts for the total solid volume without distinguishing between the volume fraction of fine particles and coarse grains. Following the contact normal fabric tensor F_c defined by Satake [22], the difference (α_c) between the maximum and the minimum eigenvalue was adopted [23] as an internal index to quantify the anisotropy degree. The succeeding 2D direct shear DEM tests revealed that α_c converged to a common plateau as the specimens reached the critical state at very large strains. In other words, the critical state should naturally have a certain degree of anisotropy. For liquefaction issues, this indicator has been applied in 2D constant-surface biaxial DEM tests [14]. With the evolution of liquefaction, two different phenomena were discovered: (i) while approaching virgin liquefaction (excess pore pressure ratio of 100%), α_c fluctuated within a certain range and its amplitude cyclically increased with the reduction in mean effective stress; (ii) by contrast, a great change in the amplitude of α_c took place as the specimen evolved through virgin liquefaction. These two facts indicate that the development of liquefaction on the specimen-scale is strongly related to the microstructural evolution.

Although the above studies have recognised the significance of fabric properties on sand response, most are restricted to idealized 2D cases. Such a definition of α_c might not be immediately suitable for 3D particles due to the lack of the following considerations. Firstly, the fabric tensor constructed for a 3D granular assembly should have three eigenvalues; however, the intermediate one is not addressed by the formula. Secondly, the scalar definition seems incapable of clarifying the complex dependency of fabric anisotropy on the loading direction and a visualization scheme displaying this dependency remains a paucity so far. One advantage of tensor analysis is to embrace the writing of mechanics laws in coordinate-free form with essential information hidden in its invariants. The primary objective of this paper is to propose a new visualization method on the basis of tensor invariants, which contributes to a comprehensive understanding of fabric anisotropy, especially for 3D granular structures. Thanks to the mathematical properties of the contact normal fabric tensor, we propose spanning a 3D principal fabric space with the three invariant eigenvectors that are orthogonal to each other. The clear benefit of this extension is to directly draw the path of fabric change in order that the dependency of induced anisotropy on the loading direction can be more intuitively mapped. As is well known, sand liquefaction occurs as a consequence of major changes in soil properties (e.g., damping ratio and shear modulus). This phenomenon is termed as cyclic degradation after Ishihara [24] and is commonly assessed with shear strain. Therefore, another objective of this paper is to deepen our knowledge about the influence of shear strain on fabric properties.

The remainder of this paper is organized as follows. The methodology adopted for DEM tests is given, followed by a comparison between the simulation results and the counterpart experiments. In the third section, the liquefaction response is assessed with two coordination numbers. In the next place, we briefly review the contact normal fabric tensor with its mathematical merits to make this work more self-contained. Subsequently, the second invariant of its deviatoric part is used to analyse the degree of anisotropy. Then, the dependency of induced anisotropy on the loading direction is shown in the principal fabric space. Finally, the relationship between fabric characteristics and the shear strain is evidenced.

2. DEM simulations and typical results

2.1. DEM simulations

3D constant-volume cyclic triaxial DEM tests were performed in this study to investigate the liquefaction response of HN31 sand ($S_iO_2>99\%$, [25]) with a mean grain size of $D_{50}=0.35$ mm and a uniformity coefficient of $C_u=D_{60}/D_{10}=1.57$. The grain size distribution curve measured by the laser diffraction method is displayed in Fig. 1. In order to mimic the material as far as possible, the identical uniformity coefficient C_u and specific gravity ($G_s=2.65$) were used in the DEM tests. To manage computation time within a reasonable range, the particle size of the DEM specimens was increased by a factor equalling to 6.5 ($D_{50}=2.28$ mm). A total of 10161 particles were generated to achieve a medium-dense state with $I_D=0.70$, as depicted in Fig. 1.

The commercial DEM programme, three-dimensional particle flow code, PFC^{3D} (Itasca Consulting Group) was employed here. In DEM simulations, the particle morphology is usually a time-consuming and expensive property to model, and so the rolling friction using spherical particles is a common substitution to express this effect [16,26]. In a granular system, the resistance of particles to rolling [27] and its associated energy dissipation during sliding might make a great contribution to the liquefaction behaviour on the macro scale. By combining the above two factors, the rolling resistance linear model [28] was adopted in this study. A series of model parameters was calibrated according to the following logic. Because the HN31 sand consists of pure silica grains, the effective modulus and stiffness ratio were set to be large enough (as

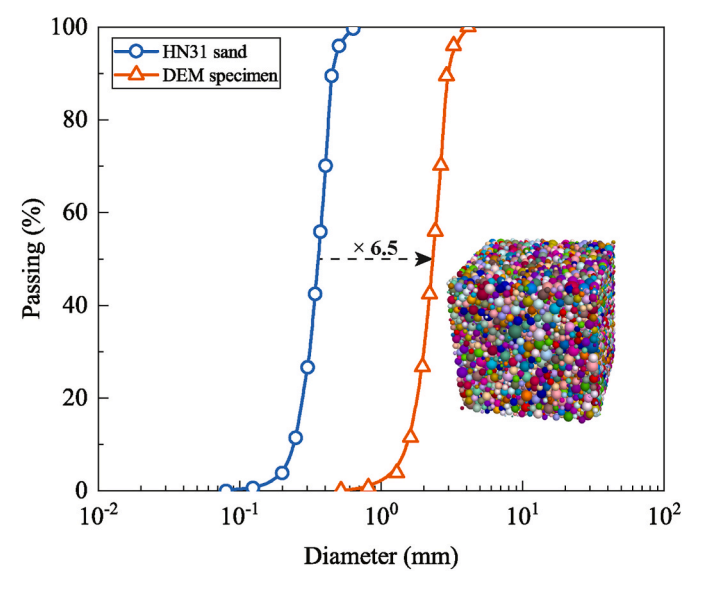


Fig. 1. Grain size distribution curve of the HN31 sand and DEM specimen.

listed in Table 1). For achieving a quasi-static condition, normal and critical damping ratio were both set to be 0.20. Finally, the rolling friction coefficient underwent a "trial-and-error" procedure to ensure that the cyclic shear resistance curve aligned with the counterpart experiments. It should be mentioned that the friction properties (i.e., μ and $\mu^{\rm r}$) for particle-facet contacts were set to zero in order that the loading facets only yielded normal forces. All particles were first generated with overlaps in an immobile cubic container (2 cm \times 2 cm \times 2 cm) consisting of six loading facets. Due to the initial overlaps, all particles were scattered throughout the container to achieve an equilibrium state. Subsequently, the loading facets were controlled by a numerical servo to impose an isotropic consolidation state of $\sigma_c^{'}=200$ kPa, as shown in Fig. 2. Finally, undrained cyclic triaxial tests with three different CSR (cyclic stress ratio, the amplitude of shear stress divided by the consolidation stress) of 0.22, 0.262, and 0.305 were simulated. In the process of shearing, the positions of four radial facets were automatically regulated through a servo function to keep the specimen volume constant. To strike a balance between calculation speed and accuracy, the time and servo step were set to be 2.5×10^{-5} s and 5.0×10^{-5} s, respectively. The local damping parameter was activated and the loading speed was set to be very low so that a quasi-static condition could be achieved. Thus, the obtained results were not influenced by the variation of these values. A quantitative discussion about this issue will be given in the next section.

2.2. Typical simulation results

The accumulation of excess pore water pressure (Δu) in terms of the number of cycles (N_{cyc}) for DEM specimens is presented in Fig. 3. It can be seen that Δu increased rapidly during the initial stage, then its growth rate gradually slowed down. While approaching liquefaction triggering with the excess pore water pressure ratio $r_{\rm u}$ ($r_{\rm u} = \Delta u/\sigma_{\rm c}$) greater than 0.8, Δu abruptly increased to match σ_c , thereby exhibiting a "doublepeak" pattern. Fig. 3 also displays stress-strain curves, revealing that the hysteresis loop initially remained flat. The negligible area enclosed by the loop implied a pseudoelastic response with minimal energy dissipation. While approaching liquefaction triggering, the hysteresis loop adopted a distinctive "reversed-Z" shape, signifying a considerable amount of energy dissipation during a single loading/unloading cycle. These features are consistent with the experimental results reported by Benahmed [29] and Zhu [30] using the same sand with $I_{\rm D}=0.70.$ For a direct comparison, the effective stress paths (deviator stress q against mean effective stress p') of the HN31 sand and the DEM specimens are provided together in Fig. 4. In response to cyclic axial loading, the effective stress paths continued moving towards the origin point and followed the "Butterfly" orbit near the final failure stage. In general, the DEM results are in good agreement with the experimental data. In geotechnical earthquake engineering, the cyclic shear resistance curve is an authentic measure to describe the liquefaction potential [31]. For the sake of simplicity, the first cycle attaining $r_{\rm u} = 1.0$ was thought of as a critical number to virgin liquefaction (N_L) . While using the constant volume method to simulate undrained shearing, the axial strain in DEM is most likely an overestimation after virgin liquefaction since the radial facets were servo-controlled to compensate the volume change. Under

Table 1 Model parameters for HN31 sand.

Linear group		particle-particle	particle-facet
Effective modulus	E*	1.0E+08	1.0E+08
Normal-to-shear stiffness ratio	K*	2.00	2.00
Friction coefficient	μ	0.43	0
Dashpot group			
Normal critical damping ratio	$\beta_{\rm n}$	0.20	0.20
Shear critical damping ratio	β_{s}	0.20	0.20
Rolling-resistance group			
Rolling friction coefficient	$\mu^{\rm r}$	0.15	0

the circumstances, the occurrence of 5% double-amplitude axial strain was adopted to define the cyclic shear resistance curves in Fig. 5. In the graph, it can be seen that two sets of data (DEM specimens vs. experiments) fall within a narrow band and can be fitted by a single trendline. While the above phenomena imply a successful calibration of model parameters, it is essential to remember that the DEM simulations were conducted differently from laboratory tests:

- The DEM specimens were assembled within a cube container (2 cm×2 cm × 2 cm) instead of a traditional cylindrical one (10 cm in diameter and 20 cm in height);
- The particles size in DEM were scaled up by a factor of 6.5 from the particle distribution curve, thereby expediting the computational speed;
- To maintain undrained shearing conditions, the side walls were adjusted to keep the total volume constant, while the axial loading was provided through the top and bottom walls.

To confirm the quasi-static condition, the inertial number I was computed, which is a dimensionless scalar to quantify the significance of dynamic effects on the flow of a granular material [32]. It can be estimated by the following equation:

$$I = \frac{|\dot{\gamma}| \cdot D_{50}}{\sqrt{P/\rho}} \tag{1}$$

where $\dot{\gamma}$ is the shear rate, D_{50} is the mean particle diameter, P is the pressure and ρ represents the density, respectively. For a clear exposition, the x-coordinates in Fig. 6 were divided by $N_{\rm L}$. Thus, $N_{\rm cyc}/N_{\rm L}=1$ referred to virgin liquefaction, as previously mentioned. In the graph, two phenomena can be identified. Prior to virgin liquefaction with $N_{\rm cyc}/N_{\rm L}=1$, I fluctuated within a very small range. After $N_{\rm cyc}/N_{\rm L}>1$, a quick growth of I can be identified owing to the triggering of liquefaction. By contrast, the inertial numbers I in all three simulations remained far away from 10^{-3} , which is the threshold value to distinguish the quasistatic flow [33] from the dense or collisional flow.

3. Discussion

For a liquefiable soil mass, the fabric characteristic linking to the state of particle spatial arrangement during the loading process is an important property to assess its macroscopic liquefaction behaviour [34]. In a general sense, different kinds of void ratios (e.g., skeleton void ratio [35] and equivalent void ratio [36]), coordination numbers [37] (or mechanical coordination numbers) and fabric tensors [15,23] can all be considered as fabric quantifications. For the constant-volume condition in this study, the void ratio remained unchanged in DEM simulations and thus put out of the scope of this section.

3.1. Coordination number

In a granular assembly, the coordination number (C_N) is defined as the average number of contacts per particle. However, certain particles can be assumed to be inactive in the state of floating identified by the number of contacts less than or equal to 1, especially after the triggering of sand liquefaction. These particles may not necessarily, upon shearing, participate in the global force chain and act almost as "void". This idea has brought a subsequent development of the mechanical coordination number ($C_{N,M}$) [38,39], in which the inactive particles are decisively disregarded while estimating the number of contacts and particles. As can be seen in Fig. 7, the initial values of C_N and $C_{N,M}$ were the same for the three simulations since all DEM specimens underwent the same isotropic consolidation state of $\sigma_c = 200$ kPa. With the progression of cyclic loading, all curves descended in a gradual manner and $C_{N,M}$ was greater than C_N because the inactive particles were not counted for the former. While arriving at virgin liquefaction with $N_{\rm cyc}/N_{\rm L} = 1$, all three

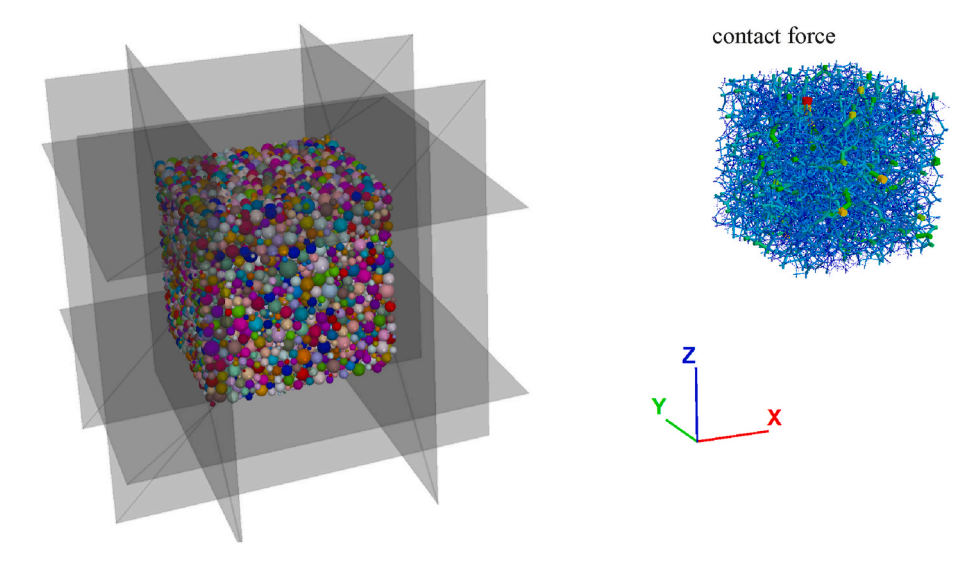


Fig. 2. Loading facets, numerical specimen and contact force system prior to undrained shearing.

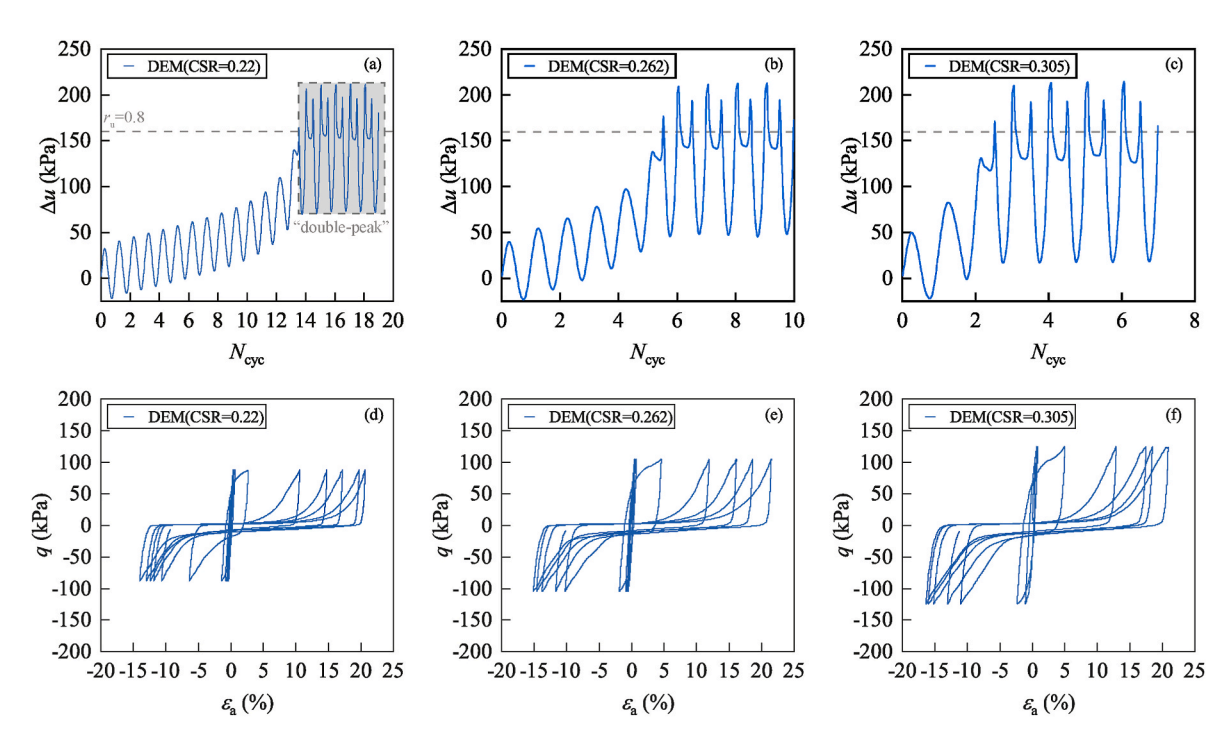


Fig. 3. Excess pore water pressure curves and stress-strain curves: (a)-(d) CSR = 0.22; (b)-(e) CSR = 0.262 and (c)-(f) CSR = 0.305.

 $C_{\rm N}$ curves decreased to around 1. In this state, open pores started emerging at inter-particle contacts points by separating them; as a consequence, most of the particles experienced a transient floating state, forming a uniform and connected porous structure [40]. In statistical terms, the value of C_N close to 1 referred to a microscopic feature that the global force chain was nearly broken (see Fig. 7a) and no contact forces could be completely transmitted. Consequently, a significant transient deformation occurred on the macro scale. In the post-liquefaction stage with $N_{\rm cvc}/N_{\rm L}>1$, sand particles should reorganize their spatial distribution and come into better contact to sustain the subsequent loading till the next liquefaction. For this reason, the time history of C_N displayed a cyclic tendency when changing the loading direction from compression to extension (or vice versa). Besides, each value of C_N close to 1 corresponded to the peak value of about $r_u = 1.0$ with the appearance of "double-peak" pattern in Fig. 3. Provided that the mechanical coordination number $C_{N,M}$ excludes the impact of

floating or inactive particles related to the liquefaction state, it cannot serve as a pertinent index to directly reveal liquefaction triggering. By contrast, this index can still represent the remaining force chain even after virgin liquefaction.

3.2. Fabric tensor

To assess the orientation of inter-particle contacts, the second-order contact normal fabric tensor F_c [22] was used. It is given by:

$$F_{c} = \frac{1}{N_{c}} \sum_{k=1}^{N_{c}} v_{c}^{k} \otimes v_{c}^{k} \tag{2}$$

where N_c is the number of contacts and v_c^k is the unit direction vector pertaining to the k^{th} contact, respectively. Because of symmetry ($F_c^T = F_c$), the fabric tensor can be orthogonally diagonalized with three ei-

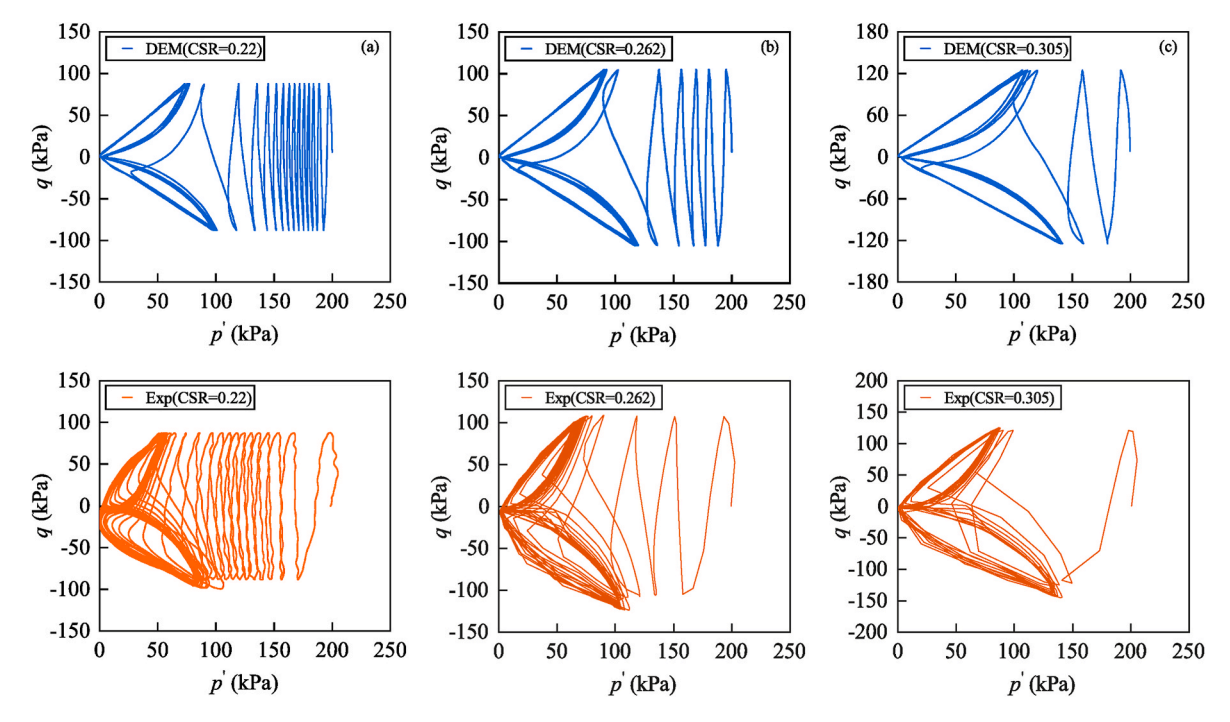


Fig. 4. Effective stress paths: (a) CSR = 0.22; (b) CSR = 0.262 and (c) CSR = 0.305 (experimental data from Refs. [29,30]).

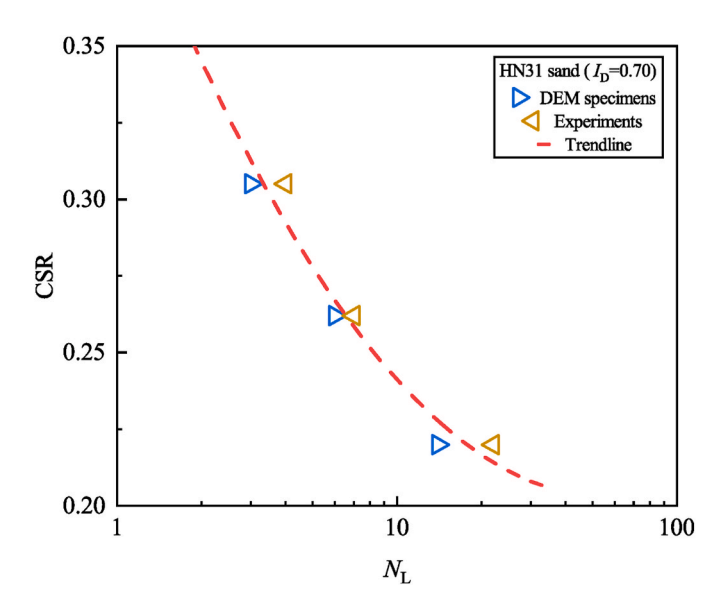


Fig. 5. Cyclic shear resistance curves of HN31 sand and DEM specimens (experimental data from Refs. [29,30]).

genvalues $(F_1, F_2 \text{ and } F_3 \in [0,1])$. The clear benefit of using unit direction vector \mathbf{v}_c^k is to force the first invariant (or the trace) of fabric tensor $I_1(F_c)$ equal to 1. This can be demonstrated as follows:

$$I_1(\mathbf{F}_c) = \frac{1}{N_c} \sum_{k=1}^{N_c} I_1(\mathbf{v}_c^k \otimes \mathbf{v}_c^k)$$
(3)

$$= \frac{1}{N_c} \sum_{k=1}^{N_c} \left(v_{c,x}^k v_{c,x}^k + v_{c,y}^k v_{c,y}^k + v_{c,z}^k v_{c,z}^k \right)$$
 (4)

where $v_{c,x}^k$, $v_{c,y}^k$ and $v_{c,z}^k$ is the projection of v_c^k on the x, y and z axis, respectively. Given the norm of v_c^k being 1, both the above equation and the sum of three eigenvalues $(F_1 + F_2 + F_3)$ are automatically equal to 1. According to the tensor analysis, the relationship between the second invariant of the fabric tensor $I_2(F_c)$ and its deviatoric part $J_2(F_c)$ can be expressed as follows:

$$\begin{cases}
J_2(\mathbf{F}_c) = \frac{1}{3} \left(I_1^2(\mathbf{F}_c) - 3I_2(\mathbf{F}_c) \right) = \frac{1}{3} - I_2(\mathbf{F}_c) \\
I_2(\mathbf{F}_c) = F_1 F_2 + F_1 F_3 + F_2 F_3
\end{cases}$$
(5)

Analogy to π plan pertaining to the principal stress space, now we can image a principal fabric space with the aforementioned condition of $F_1 + F_2 + F_3 = 1$, as shown in Fig. 8. To search for the maximum value of

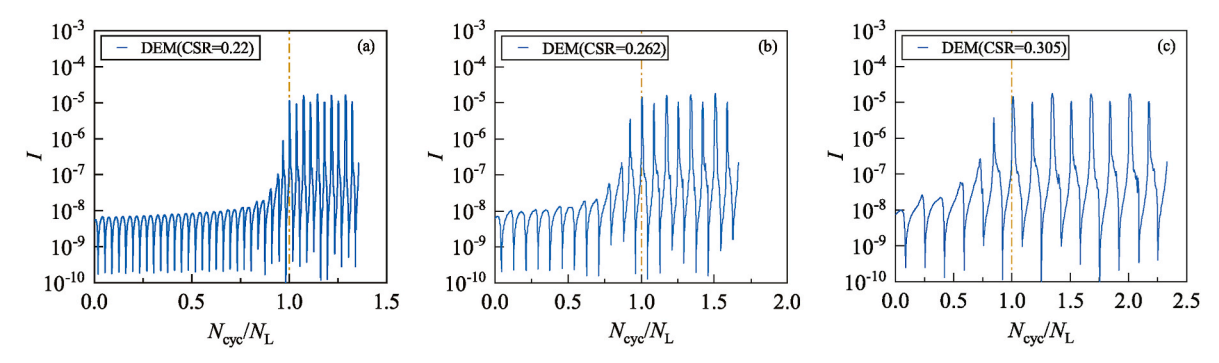
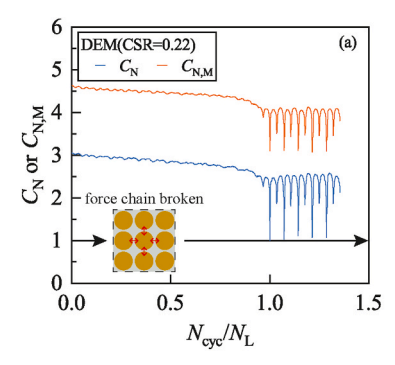
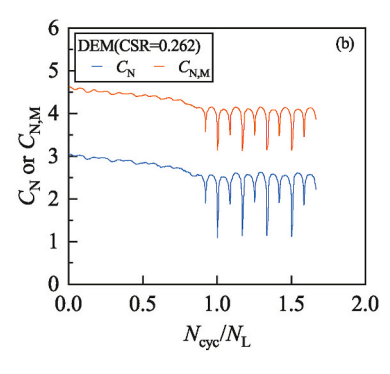


Fig. 6. Evolutions of inertia number I: (a) CSR = 0.22; (b) CSR = 0.262 and (c) CSR = 0.305.





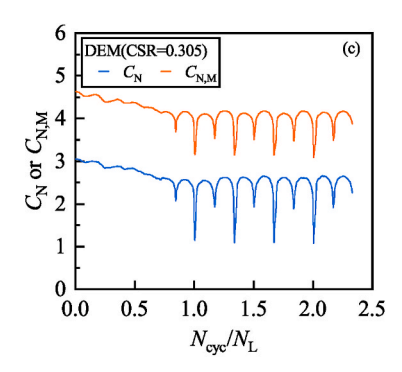


Fig. 7. Evolutions of coordination number and mechanical coordination number: (a) CSR = 0.22; (b) CSR = 0.262 and (c) CSR = 0.305.

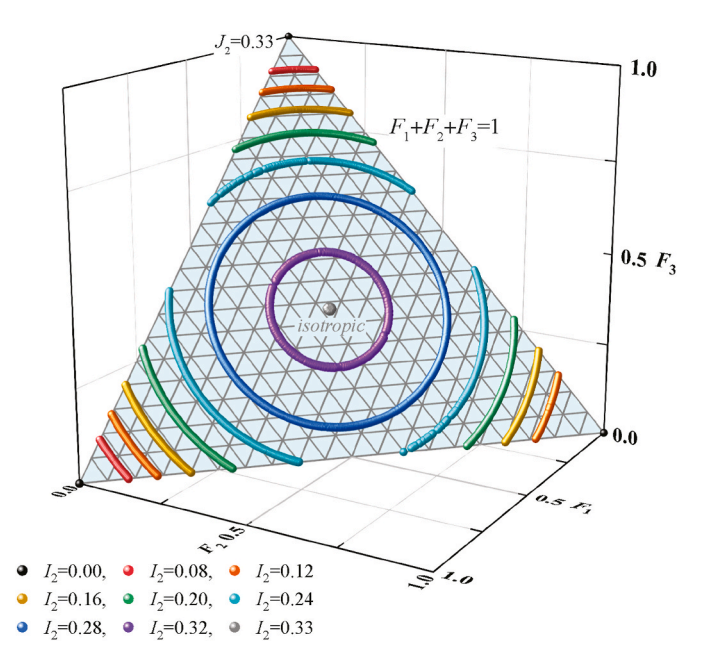


Fig. 8. Principal fabric space and contour lines of second invariant of deviatoric fabric tensor.

 $I_2(\mathbf{F}_c)$, the method of Lagrange multiplier was used with an equality constraint function $g(F_1, F_2, F_3)$:

$$\begin{cases} \nabla I_2(F_1, F_2, F_3) = \lambda \cdot \nabla g(F_1, F_2, F_3) \\ g(F_1, F_2, F_3) = F_1 + F_2 + F_3 - 1 = 0 \end{cases}$$
 (6)

where ∇ represents the Nabla differential operator and λ is the Lagrange multiplier, respectively. Following partial differentiation for each direction, the following can be obtained with three eigenvalues after diagonalization (F_1 , F_2 and F_3):

$$\begin{cases} F_{1} - axis : F_{2} + F_{3} = \lambda \\ F_{2} - axis : F_{1} + F_{3} = \lambda \\ F_{3} - axis : F_{1} + F_{2} = \lambda \end{cases}$$

$$F_{1} + F_{2} + F_{2} - 1 = 0$$

$$(7)$$

Finally, $I_2(F_c)$ reaches its maximum value of $\frac{1}{3}$ at the geometric centre with $F_1=F_2=F_3=\frac{1}{2}\lambda=\frac{1}{3}$. Under this circumstance, the fabric tensor can be simplified to $\frac{1}{3}$: δ_{ij} , where δ_{ij} is the Kronecker delta. According to Eq. (5), $J_2(F_c)$ is automatically zeroed out, standing for a theoretical isotropic state. For a clear exposition, several contour lines of $I_2(F_c)$ are directly given in Fig. 8. It can be seen that $I_2(F_c)$ sharply decreases as the fabric state moves away from the geometric centre (i.e., $F_1=F_2=F_3=\frac{1}{3}$). Hence, the second invariant of the deviatoric fabric tensor

 $J_2(F_{\rm c})$ can be thought of as an index measuring a scalar "distance" from the isotropic fabric state and its value reflects the degree of anisotropy. The maximum anisotropic state of $J_2(F_{\rm c})=\frac{1}{3}$ can be achieved at three boundary points, corresponding to an uniaxial force chain system, as displayed in Fig. 8.

Fig. 9 displays the evolutions of square root of $J_2(F_c)$ for the DEM simulations. All three curves were associated with the same initial value slightly different from 0 since a weak initial anisotropy indeed existed. Despite the fact that all DEM specimens were subjected to the isotropic consolidation state prior to applying the cyclic loading, the spatial distribution of sand particles could not be perfectly uniform throughout all DEM specimens. From a general view, $J_2(F_c)$ exhibited an accumulative growth trend as the cyclic axial stress was applied. In each compression (marked in orange) or extension half-cycle (marked in blue), the first loading stage produced a growth of anisotropy with the increase in $J_2(F_c)$ and a portion of it would be later dissipated in the following unloading stage. Another striking phenomenon revealed by Fig. 9 is that the accumulation of anisotropy was much more remarkable on the extension side than that on the compression side. A reasonable explanation for this is the dependency of stress-induced anisotropy on the loading direction. As for extension loading, the deviator stress q existed in the form of reducing the mean effective stress p, and so a weak shear strength could be expected [34], allowing an abundant development of particle arrangement. While attaining virgin liquefaction with $N_{\rm cvc}/N_{\rm L}$ = 1, the accumulated anisotropy was suddenly released, as outlined in Fig. 9. From a macroscopic viewpoint, the soil underwent a sudden loss of shear strength and behave almost as a liquid. This mechanism resulted in a temporary isotropic property, as the contact anisotropy accumulated during cyclic loading was erased due to liquefaction triggering. Similar to what has been previously observed for C_N , $J_2(F_c)$ displayed a cyclic trend since the global force chain should be regenerated in the post-liquefaction stage $(N_{\rm cyc}/N_{\rm L}>1)$ to sustain the subsequent loading.

To examine in detail the evolution of anisotropy with the build-up of sand liquefaction, the responses (CSR = 0.262) pertaining to the halfcycle before and after virgin liquefaction ($N_{\rm cyc}/N_{\rm L}=1$) are highlighted in Fig. 10, including both macroscopic $(q, p', \Delta u, \varepsilon_a)$ and microscopic ($\sqrt{J_2}$, C_N) quantities. In the graph, several gauge points (point 1 to point 6) are provided to help track changes. Owing to the continuous contractiveness induced by the foregoing loading, Δu at point 1 had already reached a high level of about $r_u = 0.8$. This high pore pressure tended to push sand particles away from one another, which can be justified by a low value of C_N . Besides, the anisotropy accumulated at point 1 was not notable since the specimen underwent an isotropic loading with $q \approx 0$. While approaching point **2**, the reduction of p required by the extension loading allowed a sufficient dilatant stage with a negative rate of Δu , during which $\sqrt{J_2}$ and C_N began to increase. This is contrary to the previous contractive stage. After this abundant dilatancy, sand particles had a more uniform inter-void system [40] to amplify the following contractiveness [41], leading to a sharp increase of Δu . As a result, the specimen was liquefied at point 3 with a very close

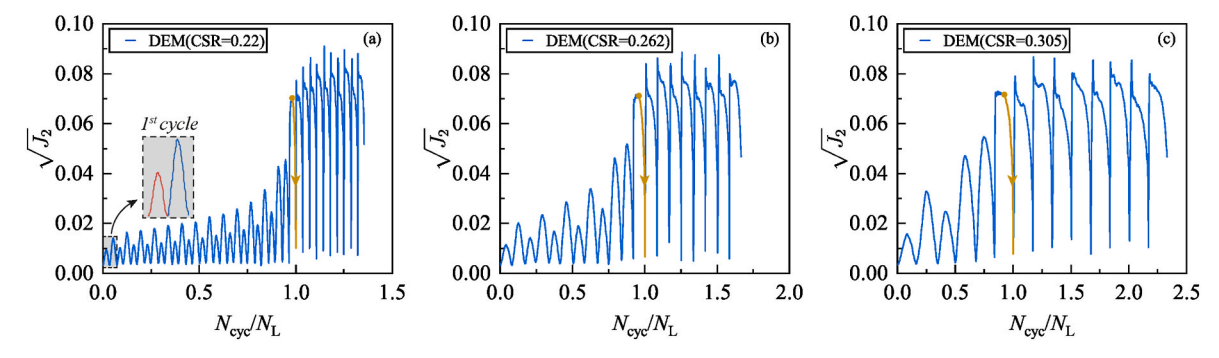


Fig. 9. Evolutions of square root of $J_2(\mathbf{F}_c)$: (a) CSR = 0.22; (b) CSR = 0.262 and (c) CSR = 0.305.

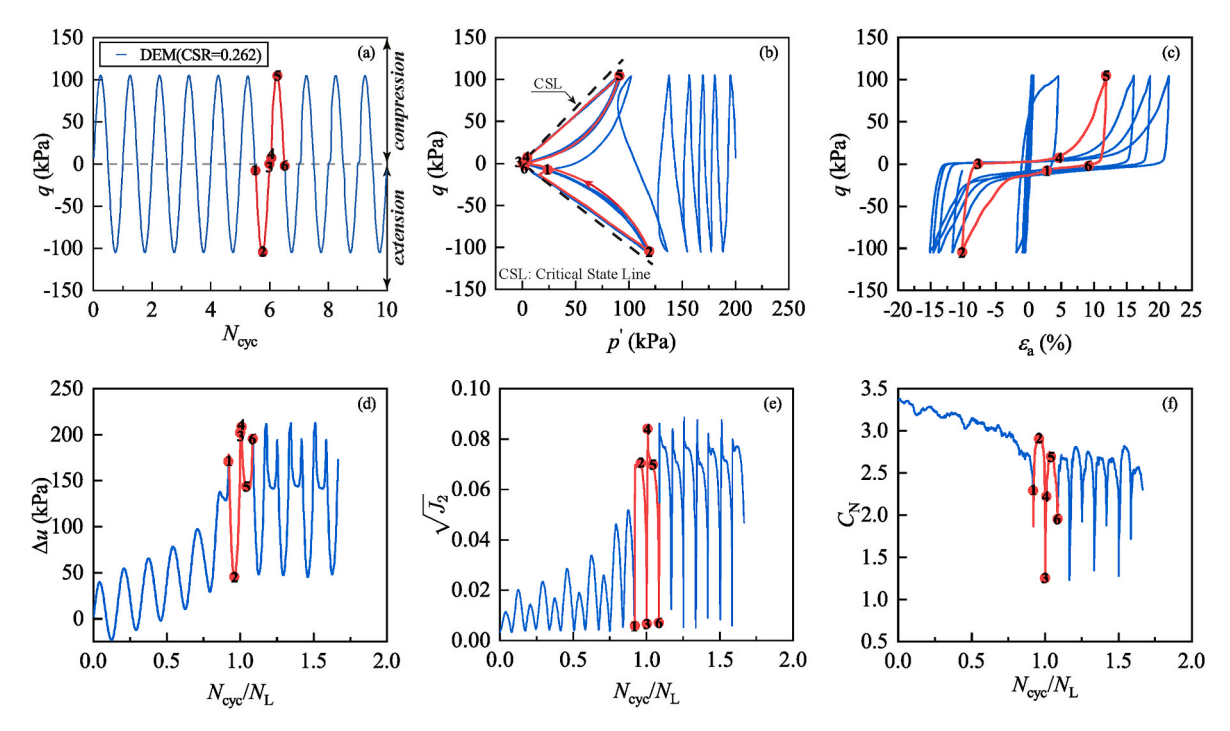


Fig. 10. Relationship between macroscopic $(q, p', \Delta u, \varepsilon_a)$ and microscopic $(\sqrt{J_2}, C_N)$ quantities near the virgin liquefaction.

value of Δu to σ_c (200 kPa). Accordingly, both C_N and $\sqrt{J_2}$ significantly decreased, referring to an isotropic and "liquid" state. In such a state, the specimen was unable to effectively yield a remarkable change of stress and pore pressure. Because of this, a quasi-zero stress state ($q \approx 0$) was thereafter maintained and only a slight growth of Δu was observed from point 3 to point 4. However, a sizable amount of ε_a was produced because of the temporary "liquid" property, as can be seen in the corresponding stress-strain curve. Subjected to this short-lived liquefaction-induced collapse, $\sqrt{J_2}$ suddenly increased in a violent manner with a few excesses. This can possibly be ascribed to the instability of the servo system, especially for this quasi-zero stress state. From point 4 to point 5, the rate of specimen deformation tended to be stabilized. At this sufficient time interval, the particle arrangement could be completely realized and the excess of $\sqrt{J_2}$ was consumed. In response to the compression loading from point 4 to point 5, the specimen kept dilating to regain its undrained shear resistance and Δu declined to the valley of the "double-peak" curve. As for the final compression unloading from point 5 to point 6, the contractiveness was enhanced again due to the abundant accumulation of dilatancy and fabric anisotropy. This led to the subsequent liquefaction at point 6; similarly, the global force chain was rebroken, manifesting an isotropic "liquid" state.

In Fig. 10, the anisotropy degrees characterizing points 2 and 5 in the

Butterfly orbit along with the critical state line [42] are very close to each other and not zero. This can be taken as reasonable if one is still reminded of the fact that the critical state itself is necessarily anisotropic [23], as mentioned in the first section. After liquefaction is reached at points 3 and 6, the contact anisotropy suddenly vanishes. From this perspective, the philosophy behind the triggering of liquefaction is in fact a cyclic process of accumulating and releasing fabric anisotropy. Fig. 11a displays the fabric paths of the three DEM simulations in the principal fabric space. In spite of different cyclic shear ratios, a unique orbit can be roughly achieved. As the deviator stress q is applied, the fabric path starts to move from the isotropic point (i.e., the geometric centre), following the direction of external loading (compression to extension and vice versa). With the progression of loading, the extent of the fabric path becomes much greater, indicating a gradual accumulation of fabric anisotropy, as conceptually shown in Fig. 11b. For a given soil fabric, there is a unique threshold value of $\sqrt{J_2}$ triggering sand liquefaction. As long as this value is reached, the specimen is liquefied. Afterwards, the fabric path immediately returns to the geometric centre (the blue-arrowed line in Fig. 11b), standing for an isotropic and liquid-like behaviour. With the variation in loading intensity (e.g., CSR in cyclic triaxial tests), the number of cycles $N_{\rm cyc}$ required for this limit might be different; however, this threshold is an intrinsic property and only fabric-dependent. In a recent DEM study [43] that included triaxial

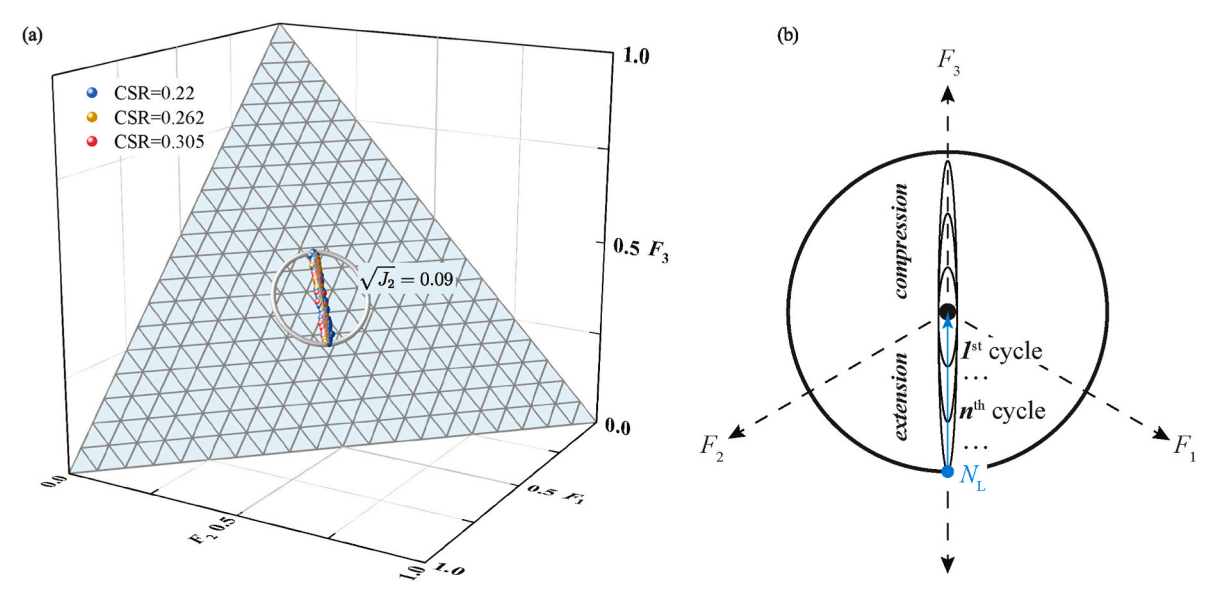


Fig. 11. (a) Fabric paths of the DEM simulations and (b) schematic of fabric path evolution to liquefaction in the principal fabric space.

drained/undrained and constant shear drained tests, it was established that the onset of flow liquefaction under monotonic loading was closely associated with a unique contact fabric. This study further confirms that the same phenomenon also prevails for cyclic mobility even under cyclic loading. It should be mentioned that the above conclusion was obtained under conventional triaxial conditions. Regarding true triaxial loading and cross-anisotropic specimens, whose bedding planes deviate from the horizontal plane, the anisotropy in contact fabric associated with liquefaction triggering may be substantially influenced by both the Lode angle and the deposit angle during preparation stage [44].

3.3. Strain dependency of fabric characteristics

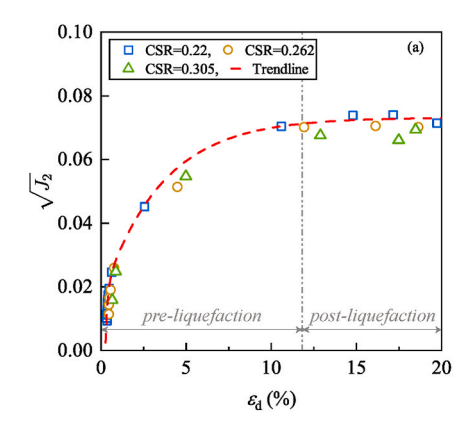
Under cyclic loading, the deformation characteristics of sand are decisively nonlinear. This is mainly reflected in the effect of cyclic degradation [24] during which the shear modulus and damping ratio vary significantly with shear strain (ϵ_d) [45,46]. Based on this, the shear strain has become widely adopted to describe the evolution of sand liquefaction. To connect the macroscopic liquefaction response with the microscopic mechanism, ϵ_d can serve as a bridge to study the evolution of fabric characteristics ($\sqrt{J_2}$ and C_N), which might be very helpful in proposing an advanced constitutive law for liquefaction modelling.

The relationship between $\varepsilon_{\rm d}$ and $\sqrt{J_2}$ is given in Fig. 12a. For a given initial state in this study ($I_{\rm D}=0.70$ and $\dot{\sigma_{\rm c}}=200$ kPa), $\varepsilon_{\rm d}$ is an effective descriptor to address the change of $\sqrt{J_2}$ since a unified trendline can be

roughly established. This is furthermore regardless of the variation in the loading intensity (CSR from 0.22 to 0.305). In the graph, the x-coordinates represent the shear strain at the maximum deviator stress $(q_{\rm max})$ of each cycle on the compression side. For a clear exposition, the shear strain triggering the virgin liquefaction is tagged to differentiate the "pre-" and "post-liquefaction" regime. In general, the curve exhibits an exponential pattern; (i) before virgin liquefaction, the degree of anisotropy sharply increases with the increase in ε_d ; (ii) after virgin liquefaction, the degree of anisotropy remains almost unchanged, corresponding to the threshold value shown in Fig. 11a. The relationship between ε_d and C_N is given in Fig. 12b. Similarly, a unified relationship can be roughly achieved for a given initial state. Before virgin liquefaction, a remarkable decrease in C_N is observed with the development of ε_d due to the continuous contractiveness. After virgin liquefaction, sand particles come into better contact, especially at the maximum deviator stress on the compression side. This leads to an increase in C_N and the regeneration of the global force chain which resists the external loading.

4. Conclusions

In this study, the evolution of fabric characteristics with the development of sand liquefaction was investigated by performing a set of DEM tests. The rolling resistance linear model was used with calibrated model parameters to fairly represent the liquefaction behaviour of HN31



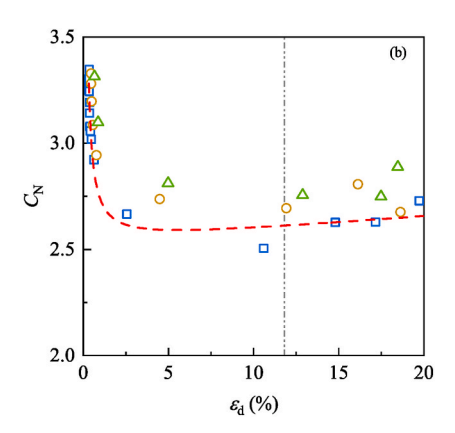


Fig. 12. Relationship between shear strain and (a) second invariant of deviatoric part of fabric tensor and (b) coordination number.

sand. The obtained DEM results can be used to derive the following conclusions:

- 1. To embody liquefaction build-up, the coordination number $C_{\rm N}$ outperforms the mechanical coordination number $C_{\rm N,M}$ since it is capable of considering the floating particles with a number of contacts less than or equal to 1, more conforming to the liquefaction state. A value of $C_{\rm N}$ close to 1 can be used to capture liquefaction triggering.
- 2. For a granular assembly, a complete insight into the orientation of inter-particle contacts can be gained with the second-order contact normal fabric tensor $F_{\rm c}$. The three eigenvectors after the diagonalization can span a principal fabric space in which the geometric centre stands for an isotropic state. The second invariant of the deviatoric fabric tensor represents a scalar "distance" from the isotropic state; thus, it can be used as an index to quantify the anisotropy degree.
- 3. Under cyclic loading in triaxial tests, the accumulation of anisotropy occurs in a gradual manner and finally leads to sand liquefaction with the attainment of an intrinsic threshold value. This value is fabric-dependent and furthermore independent of loading intensity. Regarding the principal fabric space, the relevant fabric path moves periodically around the geometric point to increase the anisotropy degree, following the direction of external loading.
- 4. Regarding a specific initial state, the shear strain ε_d describing the cyclic degradation can function as an intermediary value to establish a unified relation with both the coordination number and anisotropy degree.

Author statement

Jiajin Zhao: Investigation; Validation; Formal analysis; Writing – Original Draft; Zhehao Zhu: Conceptualization; Methodology; Writing – Review & Editing;

Dexuan Zhang: Conceptualization; Formal analysis; Hao Wang: Formal analysis; Xi Li: Formal analysis.

Declaration of competing interest

The authors declare that they have no known competing financial interests or personal relationships that could have appeared to influence the work reported in this paper.

Data availability

Data will be made available on request.

Acknowledgements

The financial supports provided by the National Natural Science Foundation of China (Grant Nos. 41931286, 41672348, 42307190) and Shanghai Sailing Program (Grant No. 21YF1432700) are deeply acknowledged.

References

- Tokimatsu K, Seed HB. Evaluation of settlements in sands due to earthquake shaking. J Geotech Eng 1987;113:861–78. https://doi.org/10.1061/(ASCE)0733-9410(1987)113:8(861).
- [2] Ishihara K, Yoshimine M. Evaluation of settlements in sand deposits following liquefaction during earthquakes. Soils Found 1992;32:178–88. https://doi.org/ 10.3208/sandf1972.32.173.
- [3] Van Ballegooy S, Malan P, Lacrosse V, Jacka ME, Cubrinovski M, Bray JD, et al. Assessment of liquefaction-induced land damage for residential Christchurch. Earthq Spectra 2014;30:31–55. https://doi.org/10.1193/031813EQS070M.
- [4] Tsukamoto Y, Ishihara K. Advances in soil liquefaction engineering. Springer; 2022.

- [5] Ye B, Lu J, Ye G. Pre-shear effect on liquefaction resistance of a Fujian sand. Soil Dynam Earthq Eng 2015;77:15–23. https://doi.org/10.1016/j. coll.tup.2015.04.08
- [6] Ye B, Hu H, Bao X, Lu P. Reliquefaction behavior of sand and its mesoscopic mechanism. Soil Dynam Earthq Eng 2018;114:12–21. https://doi.org/10.1016/j. soildyn.2018.06.024.
- [7] Ni X, Ye B, Zhang Z, Zhang S, Zhang F. An investigation of the influence of reconsolidation properties on the reliquefaction resistance of sand by element tests. J Geotech Geoenviron 2022;148(3):04021191. https://doi.org/10.1061/(asce) gt.1943-5606.0002755.
- [8] Cundall PA, Strack OD. A discrete numerical model for granular assemblies. Geotechnique 1979;29(1):47–65. https://doi.org/10.1680/geot.1980.30.3.331.
- [9] Ng TT, Dobry R. Numerical simulations of monotonic and cyclic loading of granular soil. J Geotech Eng 1994;120(2):388–403. https://doi.org/10.1061/ (ASCE)0733-9410(1994)120:2(388).
- [10] Sitharam TG, Vinod JS, Ravishankar BV. Post-liquefaction undrained monotonie behaviour of sands: experiments and DEM simulations. Geotechnique 2009;59(9): 739–49. https://doi.org/10.1680/geot.7.00040.
- [11] Gong G, Thornton C, Chan AHC. DEM simulations of undrained triaxial behavior of granular material. J Eng Mech-ASCE 2012;138(6):560–6. https://doi.org/ 10.1061/(asce)em.1943-7889.0000366.
- [12] Wang R, Fu P, Tong Z, Zhang JM, Dafalias YF. Strength anisotropy of granular material consisting of perfectly round particles. Int J Numer Anal Met 2017;41(7): 1758–78. https://doi.org/10.1002/nag.2699.
- [13] Wang R, Fu P, Zhang JM, Dafalias YF. Fabric characteristics and processes influencing the liquefaction and re-liquefaction of sand. Soil Dynam Earthq Eng 2019;125:105720. https://doi.org/10.1016/j.soildyn.2019.105720.
- [14] Wang R, Fu P, Zhang JM, Dafalias YF. DEM study of fabric features governing undrained post-liquefaction shear deformation of sand. Acta Geotech 2016;11: 1321–37. https://doi.org/10.1007/s11440-016-0499-8.
- [15] Fu P, Dafalias YF. Relationship between void- and contact normal-based fabric tensors for 2D idealized granular materials. Int J Solid Struct 2015;63:68–81. https://doi.org/10.1016/j.ijsolstr.2015.02.041.
- [16] Gu X, Zhang J, Huang X. DEM analysis of monotonic and cyclic behaviors of sand based on critical state soil mechanics framework. Comput Geotech 2020;128: 103787. https://doi.org/10.1016/j.compgeo.2020.103787.
- [17] Wei J, Wang G. Discrete-element method analysis of initial fabric effects on preand post-liquefaction behavior of sands. Géotech Lett 2017;7(2):161–6. https:// doi.org/10.1680/jgele.16.00147.
- [18] Otsubo M, Chitravel S, Kuwano R, Hanley KJ, Kyokawa H, Koseki J. Linking inherent anisotropy with liquefaction phenomena of granular materials by means of DEM analysis. Soils Found 2022;62(5):101202. https://doi.org/10.1016/j. condf.2022.101202
- [19] Yimsiri S, Soga K. DEM analysis of soil fabric effects on behaviour of sand. Geotechnique 2010;60(6):483–95. https://doi.org/10.1680/geot.2010.60.6.483.
- [20] Zuo K, Gu X, Zhang J, Wang R. Exploring packing density, critical state, and liquefaction resistance of sand-fines mixture using DEM. Comput Geotech 2023; 156:105278. https://doi.org/10.1016/j.compgeo.2023.105278.
- [21] Zhu Z, Dupla JC, Canou J, Foerster E. Experimental study of liquefaction resistance: effect of non-plastic silt content on sand matrix. Eur J Environ Civ En 2022;26:2671–89. https://doi.org/10.1080/19648189.2020.1765198.
- [22] Satake M. Fabric tensor in granular materials. 1982.
- [23] Fu P, Dafalias YF. Fabric evolution within shear bands of granular materials and its relation to critical state theory. Int J Numer Anal Met 2011;35:1918–48. https://doi.org/10.1002/nag.
- [24] Ishihara K. Soil behaviour in earthquake geotechnics. Oxford Science publications; 1995.
- [25] Zhu Z. Influence of fine particles on the liquefaction properties of a reference sandapplication to the seismic response of a sand column on a vibrating table. Springer Nature: 2023.
- [26] Wensrich CM, Katterfeld A. Rolling friction as a technique for modelling particle shape in DEM. Powder Technol 2012;217:409–17. https://doi.org/10.1016/j. powtec 2011 10 057
- [27] Yang J, Wei LM. Collapse of loose sand with the addition of fines: the role of particle shape. Geotechnique 2012;62(12):1111–25. https://doi.org/10.1680/ geot.11.P.062.
- [28] Ai J, Chen JF, Rotter JM, Ooi JY. Assessment of rolling resistance models in discrete element simulations. Powder Technol 2011;206(3):269–82. https://doi. org/10.1016/j.powtec.2010.09.030.
- [29] Benahmed N. Comportement mécanique d'un sable sous cisaillement monotone et cyclique : application aux phénomènes de liquéfaction et de mobilité clique. Ph.D Thesis. Ecole Nationale Des Ponts et Chaussées; 2001 (in French).
- [30] Zhu Z, Zhang F, Peng Q, Chabot B, Dupla JC, Canou J, et al. Development of an auto compensation system in cyclic triaxial apparatus for liquefaction analysis. Soil Dynam Earthq Eng 2021;144:106707. https://doi.org/10.1016/j. soildam.2021.106707.
- [31] Nong Z, Park SS, Jeong SW, Lee DE. Effect of cyclic loading frequency on liquefaction prediction of sand. Appl Sci-basel 2020;10(13):4502. https://doi.org/ 10.3390/app10134502.
- [32] Roux JN, Chevoir F. Discrete numerical simulation and the mechanical behavior of granular materials. Bull Lab Ponts Chaussees 2005;254:109–38.
- [33] Roux JN, Combe G. How granular materials deform in quasistatic conditions. AIP Conf Proc 2010;1227:260–70. https://doi.org/10.1063/1.3435396.
- [34] Ni X, Zhang Z, Ye B, Zhang S. Influence of anisotropy on liquefaction/ reliquefaction resistance of granular materials and its quantitative evaluation. Soil

- Dynam Earthq Eng 2022;161:107415. https://doi.org/10.1016/j.
- [35] Jefferson I, Smalley I. Fundamentals of soil behaviour. Geoderma 1994;63(3–4): 310–2. https://doi.org/10.1016/0016-7061(94)90074-4.
- [36] Thevanayagam S, Shenthan T, Mohan S, Liang J. Undrained fragility of clean sands, silty sands, and sandy silts. J Geotech Geoenviron 2002;128:849–59. https://doi.org/10.1061/(asce)1090-0241(2002)128:10(849).
- [37] Oda M. Co-ordination number and its relation to shear strength of granular material. Soils Found 1977;17(2):29–42. https://doi.org/10.3208/ sandf1972.17.2.29.
- [38] Thornton C. Numerical simulations of deviatoric shear deformation of granular media. Geotechnique 2000;50(1):43–53. https://doi.org/10.1680/ geot.2000.50.1.43.
- [39] Zhu M, Gong G, Xia J, Liu L, Wilkinson S. Effects of deviator strain histories on liquefaction of loose sand using DEM. Comput Geotech 2021;136:104213. https://doi.org/10.1016/j.compgeo.2021.104213.
- [40] Wei X, Zhang Z, Wang G, Zhang JM. DEM study of mechanism of large postliquefaction deformation of saturated sand. Yantu Lixue/Rock and Soil Mechanics 2019;40:1596–602. https://doi.org/10.16285/j.rsm.2017.2323 (in Chinese).

- [41] Nemat-Nasser S, Tobita Y. Influence of fabric on liquefaction and densification potential of cohesionless sand. Mech Mater 1982;1(1):43–62. https://doi.org/ 10.1016/0167-6636(82)90023-0.
- [42] Yang J, Wei LM, Dai BB. State variables for silty sands: global void ratio or skeleton void ratio? Soils Found 2015;55(1):99–111. https://doi.org/10.1016/j. sandf.2014.12.008.
- [43] Lashkari A, Khodadadi M, Binesh SM, Rahman MM. Instability of particulate assemblies under constant shear drained stress path: DEM approach. Int J GeoMech 2019;19(6):04019049. https://doi.org/10.1061/(asce)gm.1943-5622.0001407.
- [44] Salimi MJ, Lashkari A. Undrained true triaxial response of initially anisotropic particulate assemblies using CFM-DEM. Comput Geotech 2020;124:103509. https://doi.org/10.1016/j.compgeo.2020.103509.
- [45] Iwasaki T, Tatsuoka F, Tokida K, Yasuda S. A practical method for assessing soil liquefaction potential based on case studies at various sites in Japan. In: Proceedings of the 2nd international conference on microzonation for safer construction-research and application, San Francisco, California, USA; 1978. p. 885–96.
- [46] Kokusho T. Cyclic triaxial test of dynamic soil properties for wide strain range. Soils Found 1980;20(2):45–60. https://doi.org/10.1016/0148-9062(81)91053-6.